The Point Spread Function of the *Yohkoh* Soft X-ray Telescope

D. E. McKenzie

(Montana State University),

S. Gburek

(Space Research Centre, Polish Academy of Sciences),

L. W. Acton, P. C. Martens

(Montana State University)

ABSTRACT

The point spread function (PSF) of the *Yohkoh* solar observatory's Soft X-ray Telescope has two primary components, a sharply defined core and a diffuse wing due to photon scattering. Because the extent of the PSF is significantly wider than a single pixel, its characterization is useful for improvement of the quality of the SXT images. We will present results from analyses of the two PSF components, and demonstrate our best model of the core and scattering wing of the SXT point spread function. An example of PSF deconvolution to remove the effects of photon scattering will be given.

DETERMINATION OF PSF CORE THROUGH BLIND ITERATIVE DECONVOLUTION

Measurements of the *Yohkoh* SXT instrument response during preflight calibrations characterized the point spread function (PSF) as in Figure 1. This shows the core of the PSF, and demonstrates a dependence on position upon the CCD. Martens *et al.* (1995) constructed a model of this PSF core in terms of an elliptical generalization of the Moffat function.
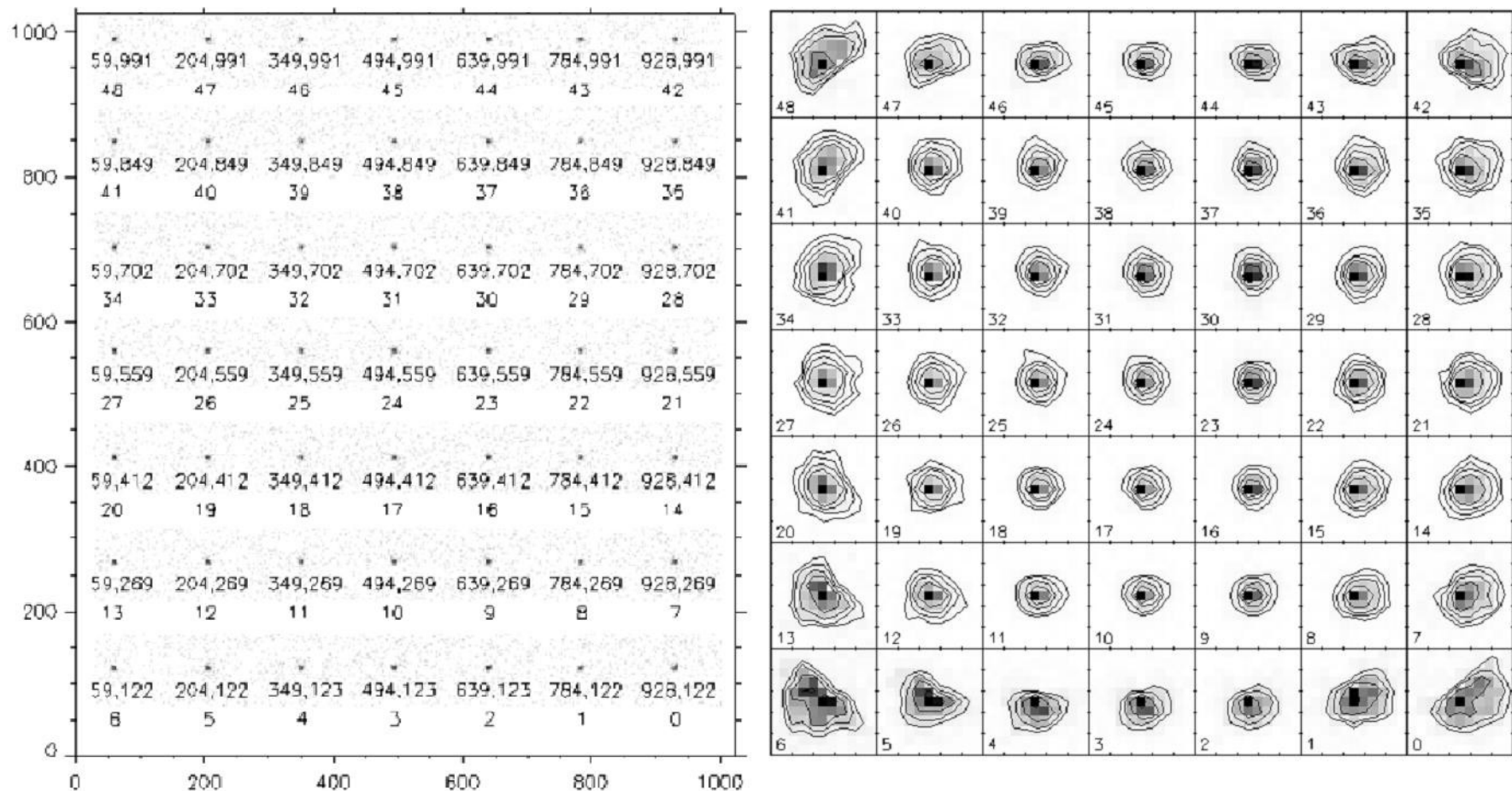
Figure 1. Pre-launch instrument calibration images from White Sands X-ray source. Images of point source shown at full size in left-hand frame; enlarged images in right-hand frame demonstrate dependence on position.

On-orbit solar flare data have been utilized to refine the model of the PSF core via Blind Iterative Deconvolution (BID, Karovska & Habbal 1991; applied to SXT, Karovska *et al.* 1994). Since the preflight calibration images show that the PSF is position-dependent, flares from many locations on the Sun should be studied. Twenty-one compact flares near positions 14-34 in Figure 1 were analyzed. For each flare, the result of the BID is a deconvolved image and a refined model of the PSF (cf Figure 2). The resultant PSFs were compared with the preflight calibration images and found to be similar, though slightly less sharp. The fuzziness may be related to the polychromatic nature of the solar radiation, compared to the monochromatic calibration radiation. Comparison of a deconvolved flare image to the raw data will be discussed below.
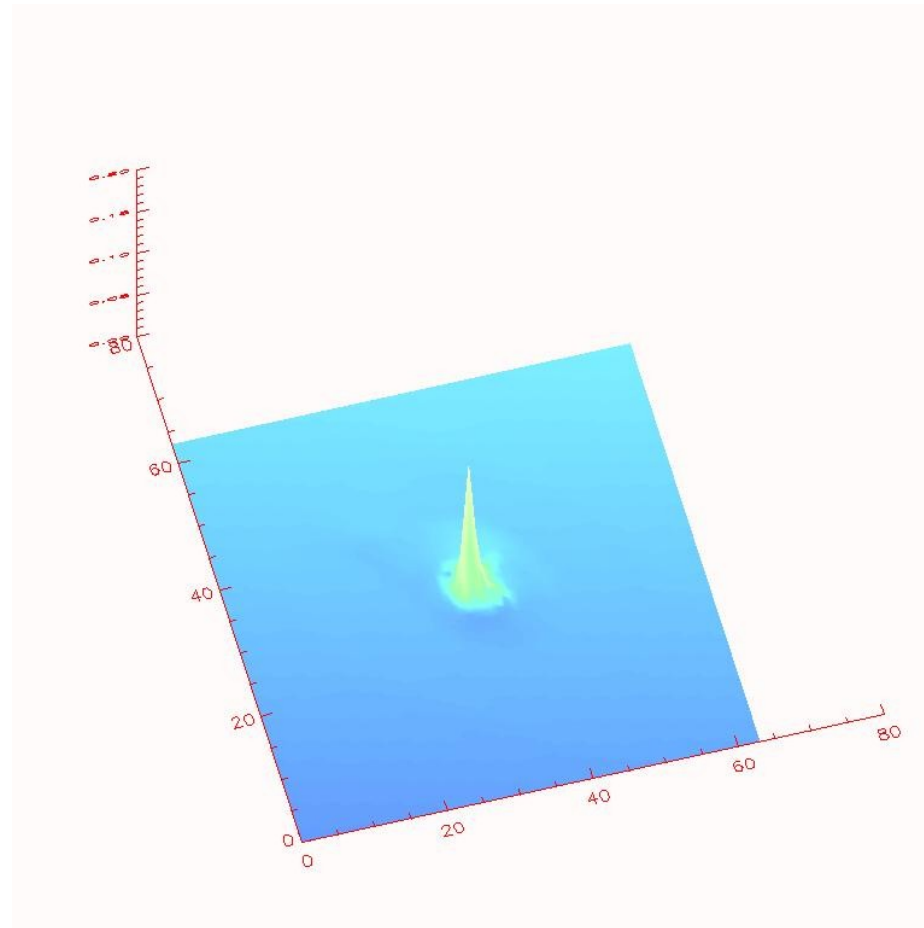
Figure 2. Refined model of the point spread function achieved from blind iterative deconvolution. Position of this flare corresponds to position #33 in Figure 1.

STRUCTURE AND SLOPE IN THE SCATTERING WINGS

The wings of the PSF include "rays", shadows of the entrance filter support. These can clearly be seen in overexposed flare images like Figure 3. Analysis of these so-called "starburst" images yield the slope of the scattering wing, as well as the contrast of signal inside/outside the "ray" shadows. The rays are included in the PSF model (Figure 4).
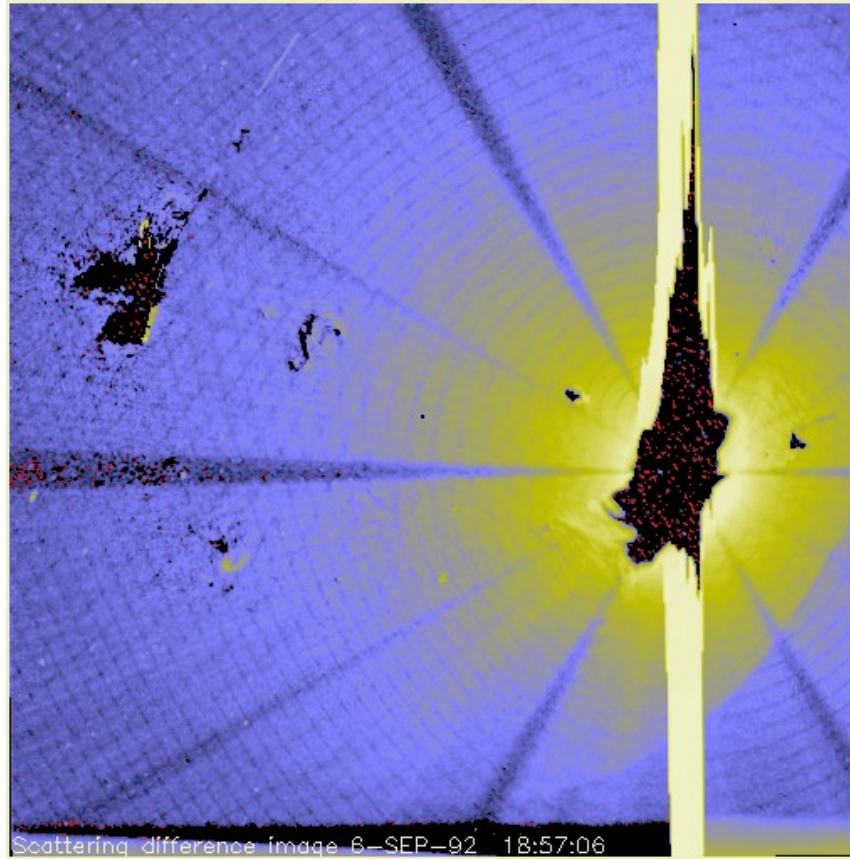
Figure 3. Difference image from before and during solar flare of 6-Sep-1992, showing the "starburst" pattern of scattered light. The dark rays emanating from the flare site are shadows of the entrance filter support.
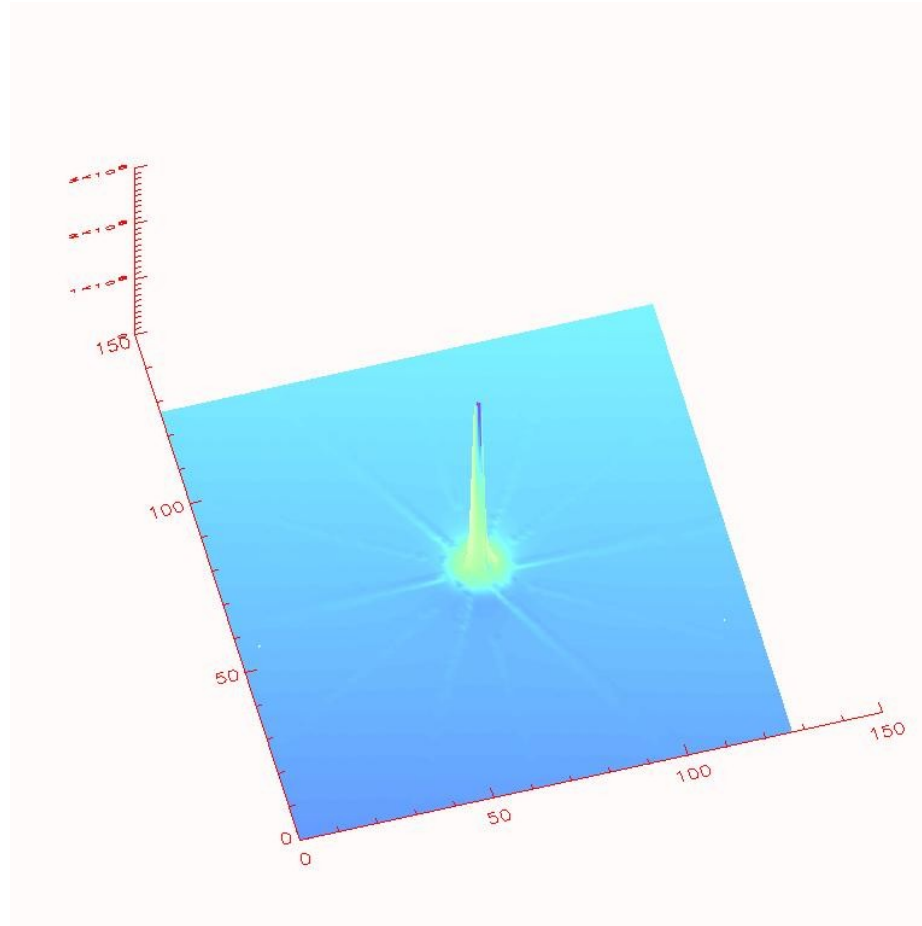
Figure 4. Model of the scattering wings of the SXT point spread function. The model includes a $1/r^2$ slope, and filter support shadows, both measured from images like Figure 3.

AMPLITUDE OF SCATTERING

The amplitude of the scattering wing is estimated from images of solar flares beyond the limb of the Sun. In such events, the assumption was made that since the flare is totally beyond the limb, any on-disk X-ray signal is due solely to scattering (cf Figure 5). This "dark disk" assumption is testable by visual inspection of the images, and by noting that in cases where the assumption is inappropriate the amount of de-scattering necessary to zero the on-disk signal is directly proportional to the exposure duration of the image. Conversely, for cases where the on-disk signal is due only (or primarily) to scattering, longer exposures reduce the amount of noise in the images; the apparent scattering amplitude thus actually decreases slightly for longer exposure durations.
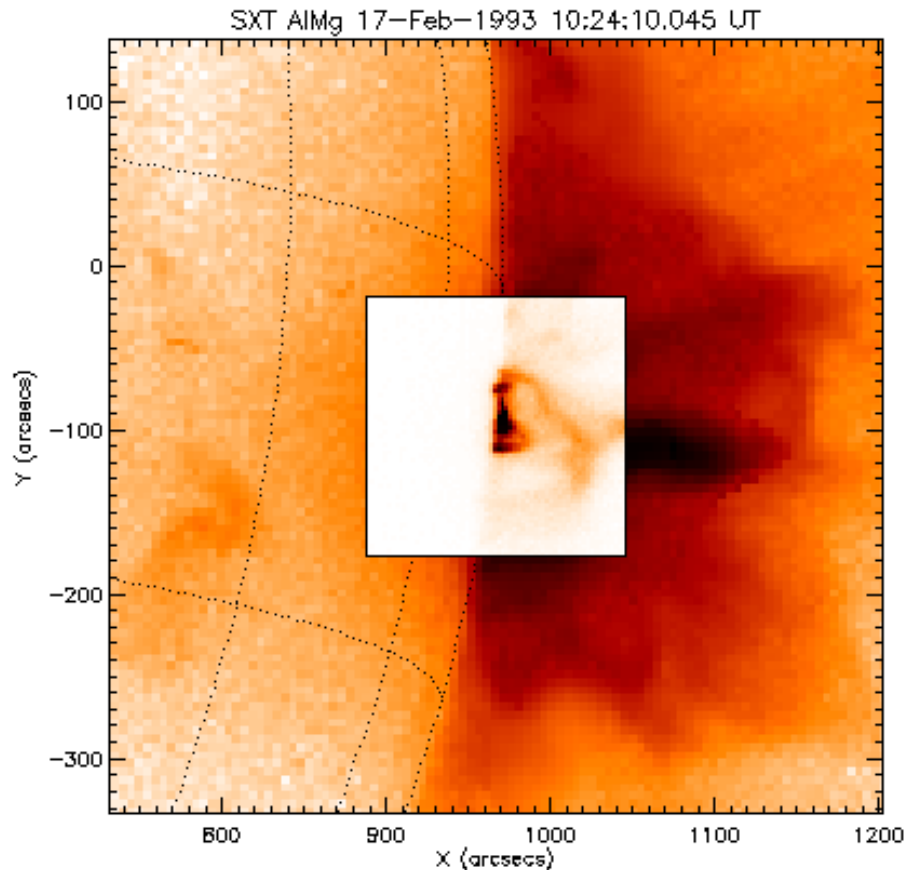
Figure 5. Example of beyond-the-limb flare used for studying the amplitude of scattering. With the flare occurring beyond the solar limb, all signal on the disk is assumed to be due to scattered light. The shorter-exposure inset demonstrates the location of the flare; the larger picture shows some scattered light on the disk, surrounding the inset. Thanks to Sam Freeland for generating a list of beyond-the-limb flares, and this image.

To estimate the amplitude of scattering, the flare images were deconvolved with iterative models of the PSF, each subsequent PSF consisting of a delta-function core plus incrementally greater amplitude of scattering wing, until the on-disk signal was reduced to a level statistically consistent with zero. Analysis of thirty-five beyond-the-limb solar flares yielded the following estimates of the scattering amplitude: in Al.1 and AlMg filters, 3-6% of the total PSF is in the wings; in Al12 and Be filters, 18-21% of the total PSF is in the wings.

DECONVOLVING THE POINT SPREAD FUNCTION FROM THE IMAGES

The point spread function can be deconvolved from the SXT images to yield improved image contrast and more accurate photometry. The deconvolved images may then be combined in the filter ratio method to yield more accurate temperature estimates. Filter ratios generated from un-deconvolved images tend to underestimate the temperatures in bright coronal structures, while simultaneously overestimating the temperatures in faint regions: degraded image intensity contrast yields degraded temperature contrast.

The Blind Iterative Deconvolution algorithm has previously been applied to *Yohkoh* SXT images (Karovska *et al.* 1994) with success. The present work extends the technique to more positions on the CCD, and makes a comparison to the pre-flight calibrations.

Similarly, a few previous attempts to correct for photon scattering within SXT have been made (Hara *et al.* 1994, Hara 1997, Foley *et al.* 1997). The studies by Hara included a more primitive model of the scattering; the work by Foley used an iterative routine to remove the effects of scattering, rather than Fourier deconvolution.

Figure 6 demonstrates the effect of deconvolution with the core PSF derived via BID. The left-hand frame shows the raw image, and the right-hand frame the result of deconvolution. (The PSF derived from BID is shown in Figure 2.) Figure 7 demonstrates the deconvolution from a PSF that includes a scattering wing; left-hand (right-hand) frame is before (after) deconvolution. In both examples, note the enhancement of contrast and improved distinction of close sources. In Figure 8, a difference image between the two sides of Figure 7, dark blue features are those which have been brightened by the deconvolution. Note especially the areas of signal depletion (white in this color table) surrounding the active regions near the east limb in Figure 8.
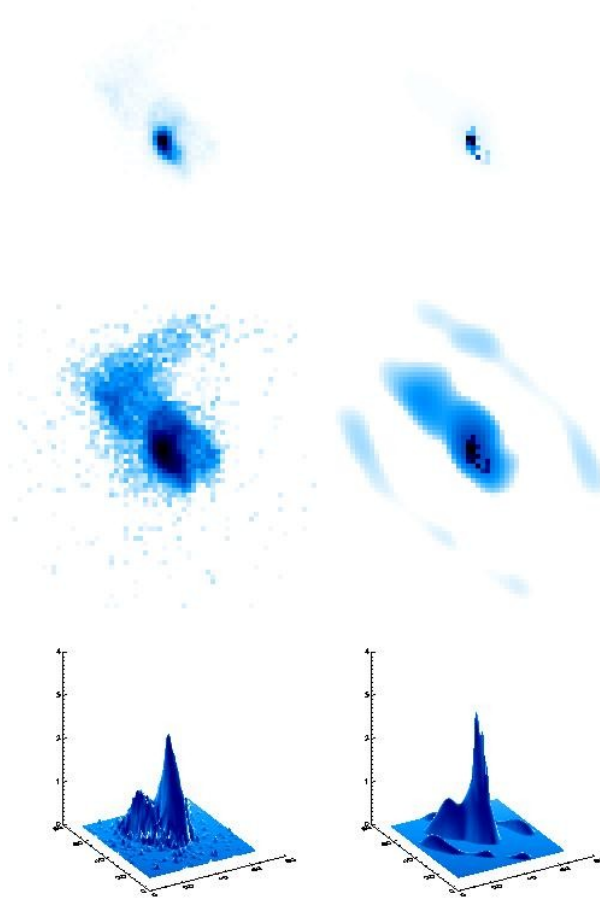
Figure 6. Deconvolution of point spread function from image of a compact flare. Left-hand frames show the raw image, right-hand frames the deconvolved image. Top to bottom: image, $\log_{10}$(image), surface plot of $\log_{10}$(image). Image contrast is enhanced, noise reduced, and sources sharpened by the deconvolution.
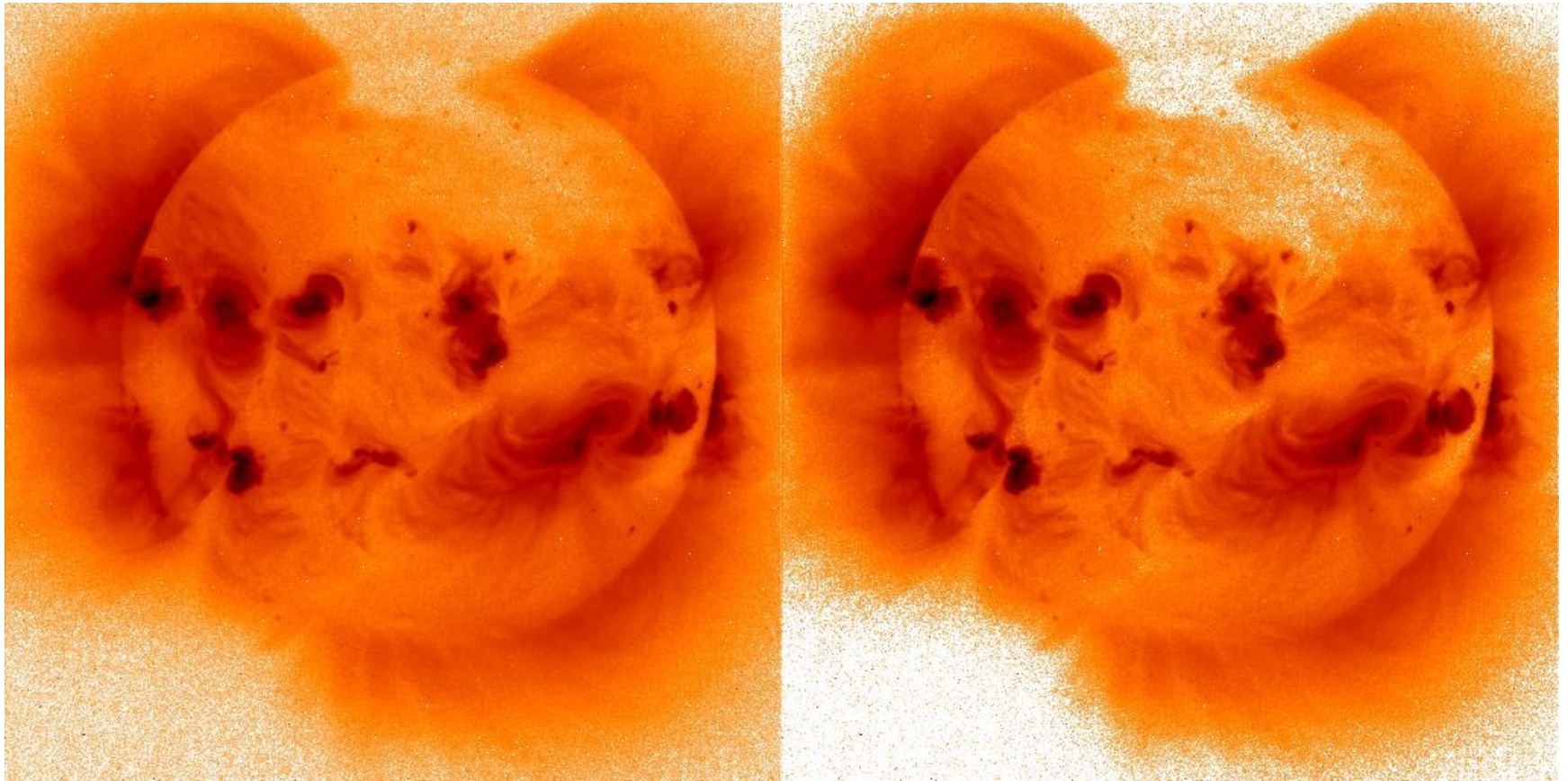
Figure 7. Example of de-scattering of full-Sun X-ray image. Left-hand frame is raw, right-hand frame is deconvolved.

Figure 8. Difference between "before" and "after" frames of Figure 7. In this color table, features with enhanced X-ray signal are dark blue, features with signals depleted by deconvolution are white.

A final example is given in Figure 9. One of the "spikey" post-eruption arcades (Svestka *et al.* 1998) with supra-arcade downflows (McKenzie 2000) is shown in AlMg and Al12 filters, both with and without deconvolution. The PSF used in this example was a delta function core plus scattering wings. The adjustment to the Al12 image is particularly obvious. The temperatures calculated via the filter ratio technique are shown in the third column; deep red represents cooler plasma, white is the hottest. Black regions in the temperature and emission measure maps are those regions where no valid filter ratio was calculable. The temperatures are in general lower after deconvolution, and the "invalid ratio" fraction of the field of view is reduced. The "hot fringe" artifact surrounding the arcade is nearly eliminated. Notably, correction for photon scattering makes possible an estimate of temperatures in the supra-arcade region.
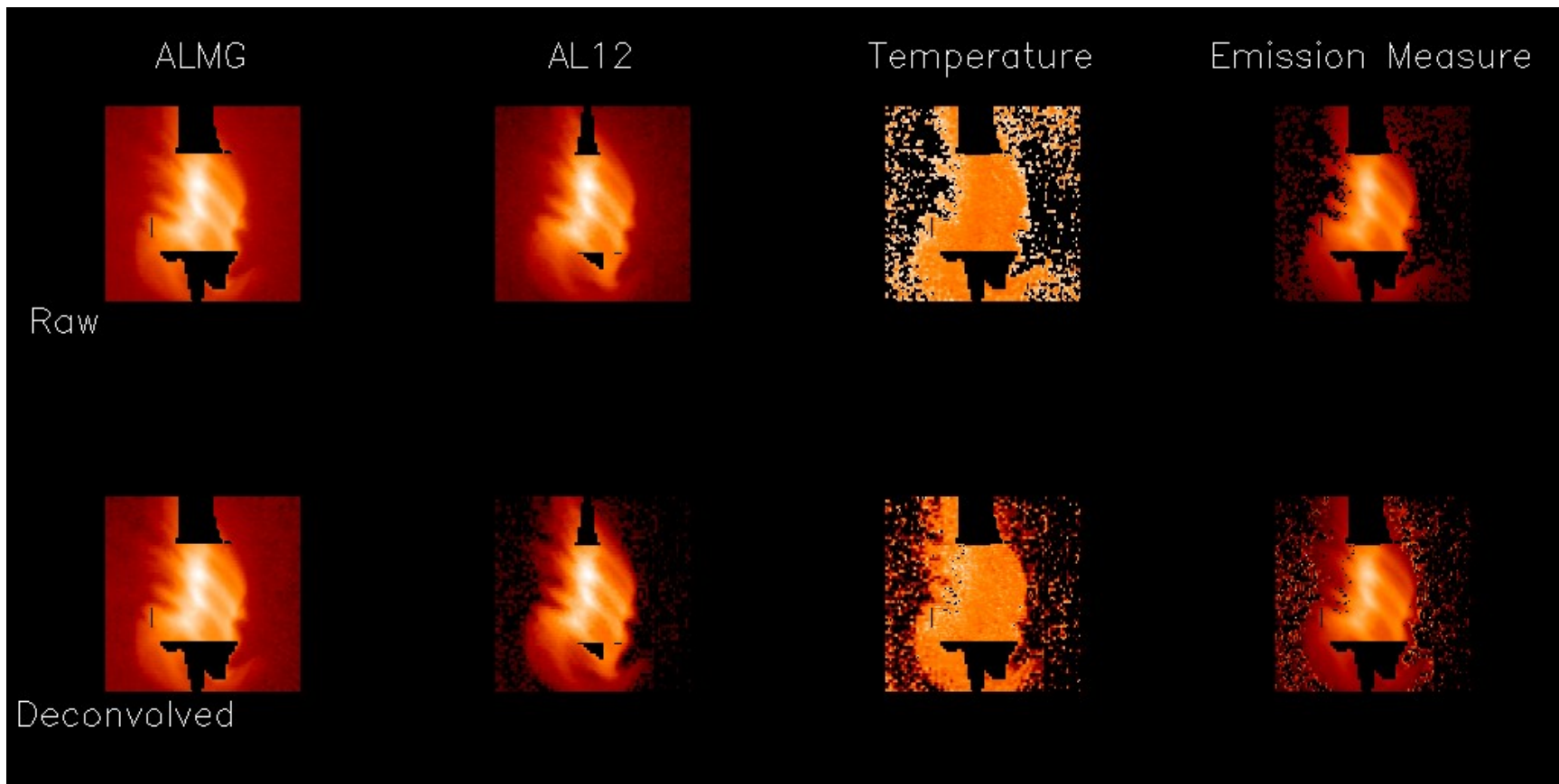
Figure 9. Example of de-scattering of flare images. Top row shows results before deconvolution, bottom row after deconvolution. Temperature map results from a ratio of signals in the Al12 and AlMg images. In temperature map, cooler plasma is shown deep red, hotter is shown yellow-white.

References

Foley, C.R., Culhane, J.L., & Acton, L.W., "Yohkoh Soft X-ray Determination of Plasma Parameters in a Polar Coronal Hole", *ApJ*, **491**, 933 (1997).

Hara, H., Tsuneta, S., Acton, L., Bruner, M., Lemen, J., & Ogawara, Y., "Temperatures of Coronal Holes Observed with the Yohkoh SXT", *PASJ*, **46**, 493 (1994).

Hara, H., "A High-Temperature Component in Coronal Holes as Confirmed by a Partial-Eclipse Observation", *PASJ*, **49**, 413 (1997).

Karovska, M., Habbal, S.R., Golub, L., DeLuca, E., & Hudson, H., "Recovering the Fine Structures in Solar Images", *Proc. of the Third SOHO Workshop – Solar Dynamic Phenomena and Solar Wind Consequences*, ESA SP-373, p.26 (1994).

Karovska, M., & Habbal, S., "High-resolution Studies of the Structure of the Solar Atmosphere Using a New Imaging Algorithm", *ApJ*, **371**, 402 (1991).

Martens, P.C., Acton, L.W., & Lemen, J.R., "The Point Spread Function of the Soft X-ray Telescope Aboard Yohkoh", *Solar Physics*, **157**, 141 (1995).

McKenzie, D.E., "Supra-Arcade Downflows in Long-Duration Solar Flare Events", *Solar Physics*, **195**, 381 (2000).

Švestka, Z., Fárník, F., Hudson, H., & Hick, P., "Large-Scale Active Coronal Phenomena in Yohkoh SXT Images – IV. Solar Wind Streams from Flaring Active Regions", *Solar Physics*, **182**, 179 (1998).